A Modeling Study of Nonstationary Trapped Mountain Lee Waves. Part II: Nonlinearity

LOUISA B. NANCE AND DALE R. DURRAN

Department of Atmospheric Sciences, University of Washington, Seattle, Washington

(Manuscript received 16 February 1996, in final form 29 August 1997)

ABSTRACT

The generation of nonstationary trapped mountain lee waves through nonlinear wave dynamics without any concomitant change in the background flow is investigated by conducting two-dimensional mountain wave simulations. These simulations demonstrate that finite-amplitude lee-wave patterns can exhibit temporal variations in local wavelength and amplitude, even when the background flow is perfectly steady. For moderate amplitudes, a nonlinear wave interaction involving the stationary trapped wave and a pair of nonstationary waves appears to be responsible for the development of nonstationary perturbations on the stationary trapped wave. This pair of nonstationary waves consists of a trapped wave and a vertically propagating wave, both having horizontal wavelengths approximately twice that of the stationary trapped wave. As the flow becomes more nonlinear, the nonstationary perturbations involve a wider spectrum of horizontal wavelengths and may dominate the overall wave pattern at wave amplitudes significantly below the threshold required to produce wave breaking. Sensitivity tests in which the wave propagation characteristics of the basic state are modified without changing the horizontal wavelength of the stationary trapped wave indicate these nonstationary perturbations are absent when the background flow does not support nonstationary trapped waves with horizontal wavelengths approximately twice that of the stationary trapped mode. These sensitivity tests also show that a second nonstationary trapped wave can assume the role of the nonstationary vertically propagating wave when the Scorer parameter in the upper layer is reduced below the threshold that will support the vertically propagating wave. In this case, a resonant triad composed of three trapped waves appears to be responsible for the development of nonstationary perturbations.

The simulations suggest that strongly nonlinear wave dynamics can generate a wider range of nonstationary trapped modes than that produced by temporal variations in the background flow. It is suggested that the irregular variations in lee-wave wavelength and amplitude observed in real atmospheric flows and the complex fluctuations above a fixed point that are occasionally found in wind profiler observations of trapped lee waves are more likely to be generated by nonlinear wave dynamics than changes in the background flow.

1. Introduction

Trapped mountain lee waves may form downstream of a mountain ridge when the Scorer parameter of the impinging flow decreases with height (Scorer 1949). Observational studies over the past three decades have revealed that trapped lee waves can exhibit three basic types of nonstationarity: 1) a gradual downstream drift of the entire lee-wave pattern (Colson and Lindsay 1959; Lindsay 1962), 2) a gradual change in the horizontal wavelength that can be as large as 30% over a time period on the order of several hours (Collis et al. 1968; Ralph et al. 1997; Sarker and Calheiros 1974; Smith 1976), and 3) temporal changes in the location and amplitude of individual crests and troughs that generate a lee-wave pattern with irregular variations in wavelength and amplitude (Brown 1983; Starr and Browning 1972). According to linear theory, a basic-state flow that is impulsively ''switched on'' and then held steady will produce lee waves in the region directly downstream of the mountain that rapidly approach a steady state (Wurtele 1955; Queney et al. 1960). The nonstationarity of observed lee waves has, therefore, often been attributed to temporal variations in the background flow (Mitchell et al. 1990; Ralph et al. 1997; Smith 1976).

Part I of this study (Nance and Durran 1997, hereafter ND97) investigated the impact of mean-flow variability on finite-amplitude trapped lee waves by conducting two-dimensional simulations of mountain waves in time-varying background flows. These simulations showed that time-dependent background flows can generate nonstationary lee-wave patterns that exhibit the three basic types of nonstationarity described above, but the timescale over which realistic changes in the background flow generate irregular variations in wavelength and amplitude appears to be significantly longer than

Corresponding author address: Dr. Louisa Bogar Nance, NOAA/National Weather Service, 7600 Sand Point Way NE, Bin C15700, Seattle, WA 98115.
E-mail: nance@seawfo.noaa.gov

TABLE 1. Characteristics of the model domain used in each two-dimensional mountain wave simulation. The mountain profile was centered at x_0.

Basic state	Domain width (km)	Domain depth (km)	x_0 (km)
REF, IJ, DJT, DJU	320	40	60
SJ, REFS, DJTS, DJS, SJS	155	15	30
Reynolds et al. (1968)	175	15	30
Shutts and Broad (1993)	180	15	30
DJU (h_0 = 600 m)	155	15	30

that necessary to account for the irregular variations in observed trapped lee waves.

This paper examines a second mechanism for the generation of nonstationarity in trapped mountain lee waves: the development of oscillations and irregularities in the lee-wave train through nonlinear wave dynamics without any concomitant change in the background flow. The amplitude of observed trapped waves is often sufficiently large that nonlinear effects may play an important role in determining the characteristics of a lee-wave pattern. Previous numerical modeling studies by Durran and Klemp (1982) and Wurtele et al. (1987) found that nonstationary lee-wave patterns may be generated by a steady background flow and that the variability increased as the height of the mountain increased. Wurtele et al. (1987) proposed that this nonstationary behavior is due to the generation of additional modes through some type of nonlinear interaction. As will be demonstrated, nonlinear wave dynamics can indeed generate irregular variations in a lee-wave train, and these variations can develop far more rapidly than those forced by realistic changes in the upstream flow. As a consequence, it appears that the irregular variations observed in some atmospheric lee waves may be produced by nonlinearity rather than temporal variations in the background flow.

2. Model description

The numerical model used in this study is based on the fully compressible numerical model developed by Durran and Klemp (1983), which is designed to calculate two-dimensional, high Rossby number airflow ($f \rightarrow 0$) over an infinitely long uniform mountain barrier. Details of the model are described in ND97. The numerical simulations in this study were computed on a model domain with a vertical grid spacing of 200 m and a horizontal grid spacing of 500 m. The small time step was 1 s, and the large time step was 4 s. The domain configurations used in each simulation are summarized in Table 1. A wider domain was used for longer simulation times or basic-state profiles that generate stationary trapped waves with higher group velocities in order to avoid problems with the downstream lateral boundary condition. The radiation boundary condition of Klemp and Durran (1983) and Bougeault (1983) was applied at the top of the model domain, and a weak version of the wave-absorbing layer described in Durran and Klemp (1982) was applied over the top 10 km of the deeper domains to ensure the disturbance arriving at the upper boundary was sufficiently weak that it could be transmitted through the upper boundary with minimal error. The topography was specified using a Witch of Agnesi profile with a half-width, b, of 3 km centered at x_0 (see Table 1). The model was initialized with a hydrostatically balanced, horizontally uniform basic state, and the gravity wave transients generated during the initialization were reduced by gradually increasing the horizontal wind profile, $\overline{u}(z)$, and gravitational constant from zero to their specified values over the time periods t_u and t_g such that $\overline{u}(0)t_u/b = 1$ and $\overline{u}(0)t_g/b = 4$.

3. Idealized two-layer atmospheric profiles

a. The nonlinear breakdown of a stationary trapped wave

The influence of nonlinear wave dynamics on the stationarity of trapped mountain lee waves is examined by comparing numerical simulations for flow over mountains 1 and 385 m high. In both simulations, the background flow was steady with a constant wind speed of 10 m s^{-1} and a two-layer static stability profile,

$$N = \begin{cases} N_l, & 0 \le z \le d \\ N_u, & z > d, \end{cases}$$

in which $N_l = 0.01007$ s^{-1}, $N_u = 0.00316$ s^{-1}, and $d = 3$ km. Since the Scorer parameter for a compressible fluid can be well approximated as $l^2 = N^2/\overline{u}^2$ when $\overline{u}$ is constant with height (Nance 1997), this basic state has the two-layer, constant Scorer parameter configuration used by Scorer (1949) to obtain a linear solution for stationary trapped lee waves downstream of a Witch of Agnesi mountain profile. Equation (16) in Scorer (1949) predicts that this atmospheric profile, hereafter referred to as the reference profile or "REF," will generate stationary trapped lee waves with a horizontal wavenumber (k_s) of 6.75×10^{-4} m^{-1}. ND97 noted that this type of two-layer atmospheric profile will also support nonstationary trapped waves with intrinsic frequencies in the range $N_u < |\tilde{\omega}| < N_l$, where $\tilde{\omega} = (c - \overline{u})k$ and c is the phase speed of the disturbance.

The lee waves produced by flow over the 1- and 385-m mountains are compared in Fig. 1, which shows contours of the vertical velocity fields in the x–z plane at $t = 7$ h. The contour interval used in each panel has been scaled to reflect the dependence of the linear trapped lee-wave solution on mountain height. In other words, Figs. 1a and 1b would be identical if nonlinear processes were not influencing either solution. The lee-wave pattern produced by the 1-m mountain exhibits slight variations in the amplitude of adjacent waves, whereas the waves generated by the 385-m mountain exhibit pronounced variations in both wavelength and

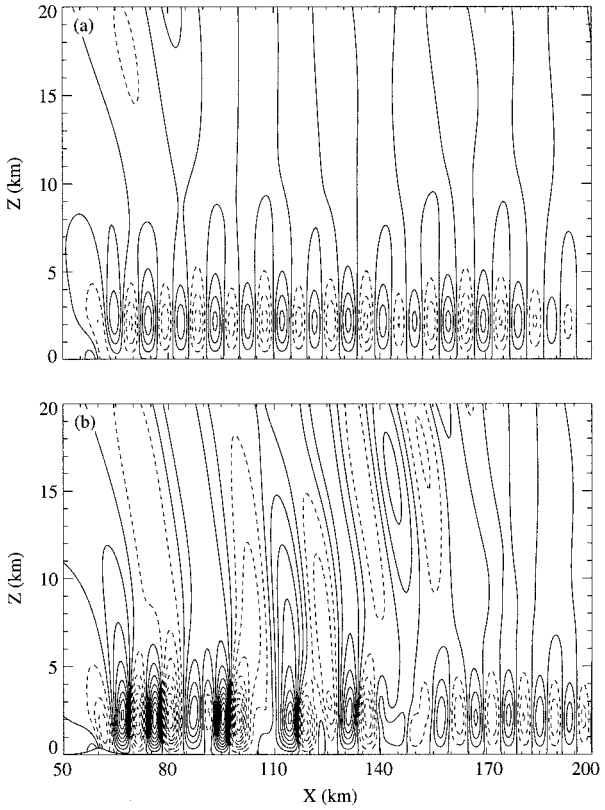

FIG. 1. Contour plots of the vertical velocity fields in the x–z plane at $t = 7$ h for the REF profile and a mountain height of (a) 1 m (contour interval: 0.0013 m s^{-1}) and (b) 385 m (contour interval: 0.5 m s^{-1}).

amplitude. Another important difference between these two simulations is the source of the vertically propagating waves that appear in the upper layer ($z > 3$ km). Since the Scorer parameter in the upper layer of the REF basic state is greater than zero, the cross-mountain flow generates stationary waves that propagate vertically through both layers of the fluid. These waves appear in a wedge-shaped region whose downstream boundary lies approximately along a line between the mountain ridge and the point $x = 90$ km, $z = 20$ km in Fig. 1. In addition to the waves forced directly by the mountain, vertically propagating waves also appear in the 385-m mountain simulation above the region 100 km $< x <$ 170 km. These vertically propagating waves, which are not present in the 1-m mountain simulation, appear to emanate from the portion of the lee-wave train that exhibits the largest variability.

The lee waves downstream of the 385-m mountain exhibit very regular temporal variations in the region 85 km $\leq x \leq$ 105 km. The characteristics of these variations are illustrated in Fig. 2, which shows a time series of the 460-K isentrope at 20-min intervals. The individual crests and troughs trace an elliptical pattern such that the oscillations of adjacent crests and troughs are 180 degrees out of phase, which, in turn, suggests these oscillations are generated by a superposition of the stationary trapped wave and a nonstationary disturbance with a horizontal wavelength approximately twice that of the stationary trapped wave. In those regions where the nonstationarity is most pronounced, adjacent waves appear to merge at times. Starr and Browning

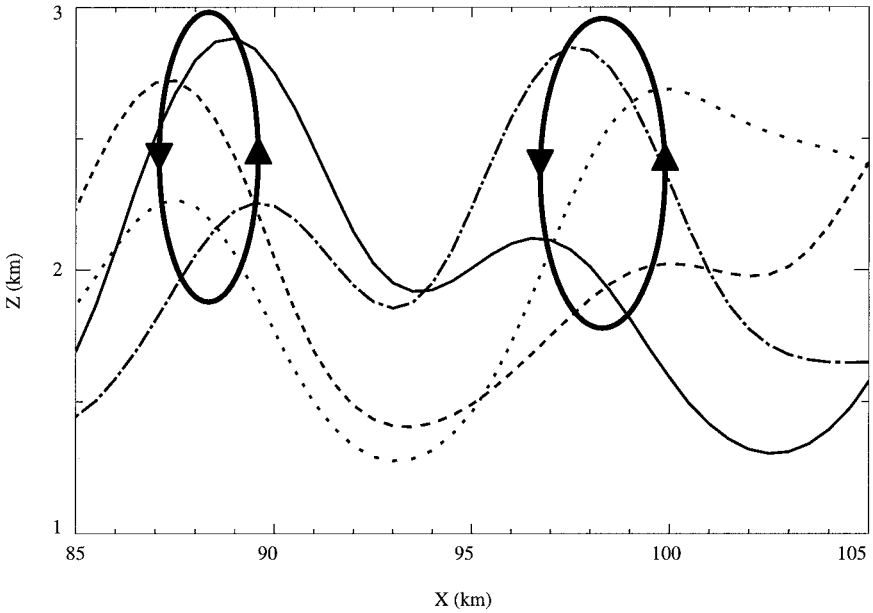

FIG. 2. Plot of the 460-K potential temperature isentrope at 20-min intervals for the REF profile and a 385-m mountain. The solid line corresponds to the earliest time and is followed by the long-dashed, short-dashed, and dash-dotted curves, in that order. Two ellipses have been overlaid to indicate the path traced by each crest in the lee-wave pattern. The arrows indicate the direction the crests are moving around each ellipse.

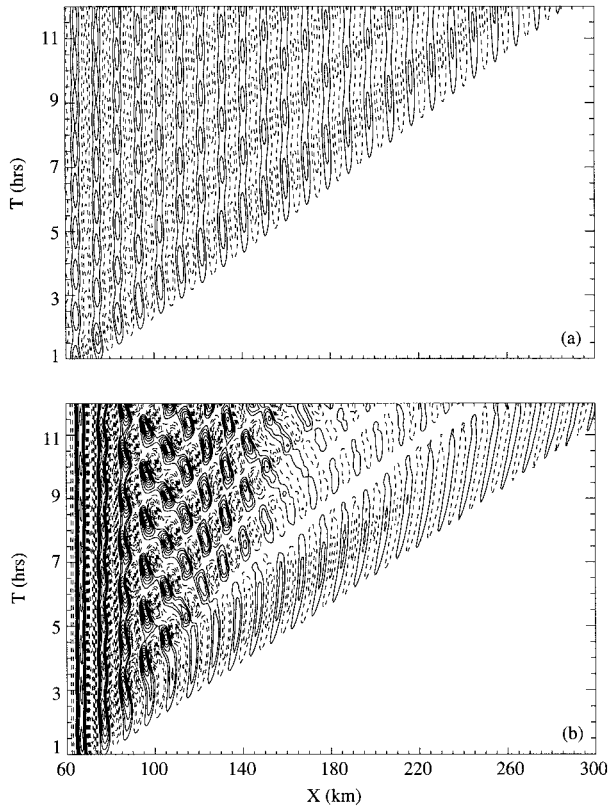

FIG. 3. Contour plots of the vertical velocity fields in the x–t plane at $z = 2$ km for the REF profile and a mountain height of (a) 1 m (contour interval: 0.0018 m s^{-1}) and (b) 385 m (contour interval: 0.7 m s^{-1}). The zero contour has been omitted for clarity.

(1972) observed an unsteady lee-wave event downstream of the Welsh mountains on 3 February 1970. As shown in their Fig. 7, an individual wave crest is observed to break down into two separate crests between 1200 and 1300 UTC. Two crests farther downstream appear to merge between 1300 and 1400 UTC. The evolution of the waves observed by Starr and Browning qualitatively resembles the behavior of the lee waves in this finite-amplitude mountain wave simulation.

The evolution of the lee waves in these two simulations is compared in Fig. 3, which shows contours of the vertical velocity downstream of the mountain in the x–t plane at $z = 2$ km. The contour interval used in each panel has once again been scaled in proportion to the amplitude of the linear solution generated by each mountain height. For a mountain height of 1 m, the spatial locations of the crests and troughs in the lee-wave pattern remain almost stationary, but the amplitudes of these waves undergo an oscillation that slowly decays with time. This oscillation originates at the upstream edge of the lee-wave pattern and propagates through the lee waves downstream at a group velocity similar to that of the stationary trapped mode. A similar slowly decaying transient is also present in a solution to the linearized, time-dependent equation governing Boussinesq flow,

$$(w_{xx} + w_{zz})_{TT} - \overline{u}_{zz} w_{xT} + N^2 w_{xx} = 0, \qquad (1)$$

where

$$(\,)_T = \frac{\partial}{\partial t} + \overline{u}\frac{\partial}{\partial x},$$

obtained for the same atmospheric profile using the semi-analytic model described in Pandya and Durran (1996). The similarity between the linear solution and that obtained using a 1-m mountain in the full numerical model demonstrates that the slowly decaying transient is not an artifact of the numerical model. The transient behavior in these time-dependent trapped lee-wave solutions is also consistent with the transient development of deep-water lee waves in the linear analytic solution derived by Wurtele (1955).

When the mountain height is increased to 385 m, the amplitude of the oscillation near the mountain becomes less pronounced (i.e., the transients due to the startup of the numerical model are a smaller percentage of the total amplitude), whereas rather pronounced temporal oscillations develop in both the position and the amplitude of the crests and troughs in the region 80 km $\leq x \leq$ 180 km (Fig. 3b). These oscillations are dominated by a disturbance with an upstream phase speed superimposed on the stationary lee wave. Also note that the amplitude of all waves downstream of $x = 160$ km is significantly weaker than that of the waves immediately downstream of the mountain ridge. Since the energy associated with the stationary trapped wave propagates horizontally downstream of the mountain, the downstream reduction in wave amplitude suggests that energy has been removed from individual trapped wave packets as they propagate downstream.

The vertical structure and propagation characteristics of the disturbances in the region of maximum lee-wave variability are illustrated in Fig. 4, which shows contours of the vertical velocity field downstream of the mountain in the x–t plane at three different elevations: $z = 2$ km, $z = 9$ km, and $z = 15$ km. At low levels, a disturbance with an upstream phase speed of approximately -4.1 m s^{-1} is superimposed on the stationary trapped wave (Fig. 4c). The stationary and upstream propagating components of the wave pattern decay with height, whereas a wave with a downstream phase speed of approximately 3.3 m s^{-1} becomes more prominent at upper levels (see Figs. 4a,b). As determined from Fig. 4b, the horizontal wavenumber and frequency associated with the upstream propagating disturbance are approximately 2.9×10^{-4} m^{-1} and -0.0012 s^{-1}, whereas the horizontal wavenumber and frequency associated with the downstream propagating disturbance are approximately 3.7×10^{-4} m^{-1} and 0.0012 s^{-1}. The upstream propagating wave decays more gradually with height in the upper layer than the stationary wave, consistent with the vertical decay scales predicted by linear

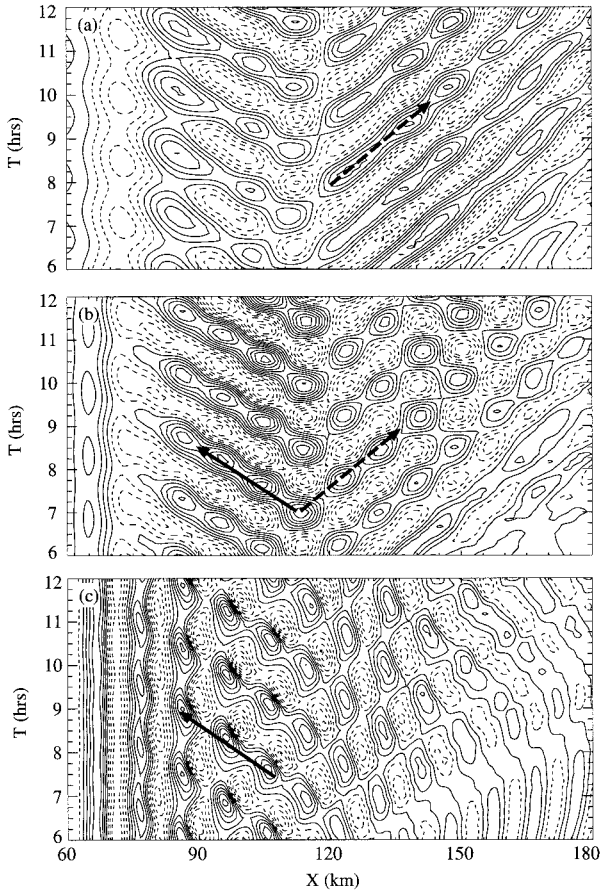

FIG. 4. Contour plots of the vertical velocity fields in the x–t plane at (a) $z = 2$ km (contour interval: 1 m s^{-1}), (b) $z = 9$ km (contour interval: 0.25 m s^{-1}), and (c) $z = 15$ km (contour interval: 0.25 m s^{-1}) for the REF profile and a mountain height of 385 m. The solid and dashed arrows indicate phase speeds of -4.1 and 3.3 m s^{-1}, respectively.

theory for nonstationary trapped waves. Thus, the disturbance in this region appears to be primarily composed of three waves: a stationary trapped wave that is the finite-amplitude equivalent of the linear resonant mode, a nonstationary trapped wave with an upstream phase speed, and a nonstationary vertically propagating gravity wave with a downstream phase speed.

The characteristics of these three modes come close to meeting the conditions for a classic resonant triad interaction. In particular, the wavenumbers and the frequencies of the simulated modes approximately satisfy the resonance criteria of Hasselmann (1967), which states that the nonlinear coupling between two infinitesimal components 1 and 2 and a finite component 0 will be unstable if the wavenumbers and frequencies of these components satisfy the conditions

$$\mathbf{k}_1 + \mathbf{k}_2 = \mathbf{k}_0, \tag{2}$$

and

$$\omega(\mathbf{k}_1) + \omega(\mathbf{k}_2) = \omega(\mathbf{k}_0). \tag{3}$$

In the above, $\mathbf{k}_i$ represents the wavenumber vector of the ith wave, and $\omega(\mathbf{k}_i)$ represents the frequency defined by the linear dispersion relation for internal gravity waves. Let the subscripts 0, 1, and 2 correspond, respectively, to the stationary trapped wave, the nonstationary trapped wave, and the nonstationary vertically propagating wave. The horizontal wavenumbers (in 10^{-4} m^{-1}) satisfy

$$2.9 + 3.7 \approx 6.7,$$

and the frequencies (in 10^{-3} s^{-1}) satisfy

$$-1.2 + 1.2 = 0.$$

It is virtually impossible to determine the vertical wavenumbers of the trapped waves in the lower layer directly from the numerical data. Linear theory for Boussinesq gravity waves was, therefore, used to estimate the vertical wavenumbers for all three waves using the preceding horizontal wavenumbers and frequencies. The triad criteria for the vertical wavenumber (in 10^{-4} m^{-1}) in the lower layer obtained in this manner is

$$-6.5 + 14.4 \approx 7.5.$$

The sign of m_2 is determined by the requirement that the vertically propagating wave carry energy upward and by the nonnegativity of ω_2 and k_2. The signs of m_0 and m_1 cannot be determined from the dispersion relation a priori since these are trapped waves. The signs of m_0 and m_1 were simply chosen such that the triad criteria for the vertical wavenumber is approximately satisfied in the lower layer. In summary, the observed modes satisfy the resonant interaction criteria to within $\pm 3\%$ of the largest term in each of (2) and (3).

There are, however, certain aspects of this problem that set it apart from the simplest theories of wave–wave interactions. In particular, one of the nonlinearly interacting waves does not satisfy the surface boundary condition downstream of the mountain ($w = 0$), which is to say that one of the three modes involved in the triad is not a free mode of the first-order (linear) problem. A second complication is that these waves are continually forced as energy is imparted to the stationary trapped wave by the mountain, and then a portion of this energy is removed by the nonlinear interactions that feed energy into the vertically propagating wave. As a consequence, it is difficult to formally evaluate the second-order interactions.

Although a complete mathematical analysis of these wave–wave interactions is beyond the scope of this paper, viewing the evolution of the lee-wave pattern in this simulation in terms of horizontal wavenumber spectra does suggest one way that the classic theory could be generalized to better describe the behavior of these waves. Horizontal wavenumber spectra were computed using the vertical velocities from the 385-m mountain simulation at each vertical level over the region 90 km $\leq x \leq$ 180 km. The details of this spectral analysis are described in the appendix. Contour plots of the spectral

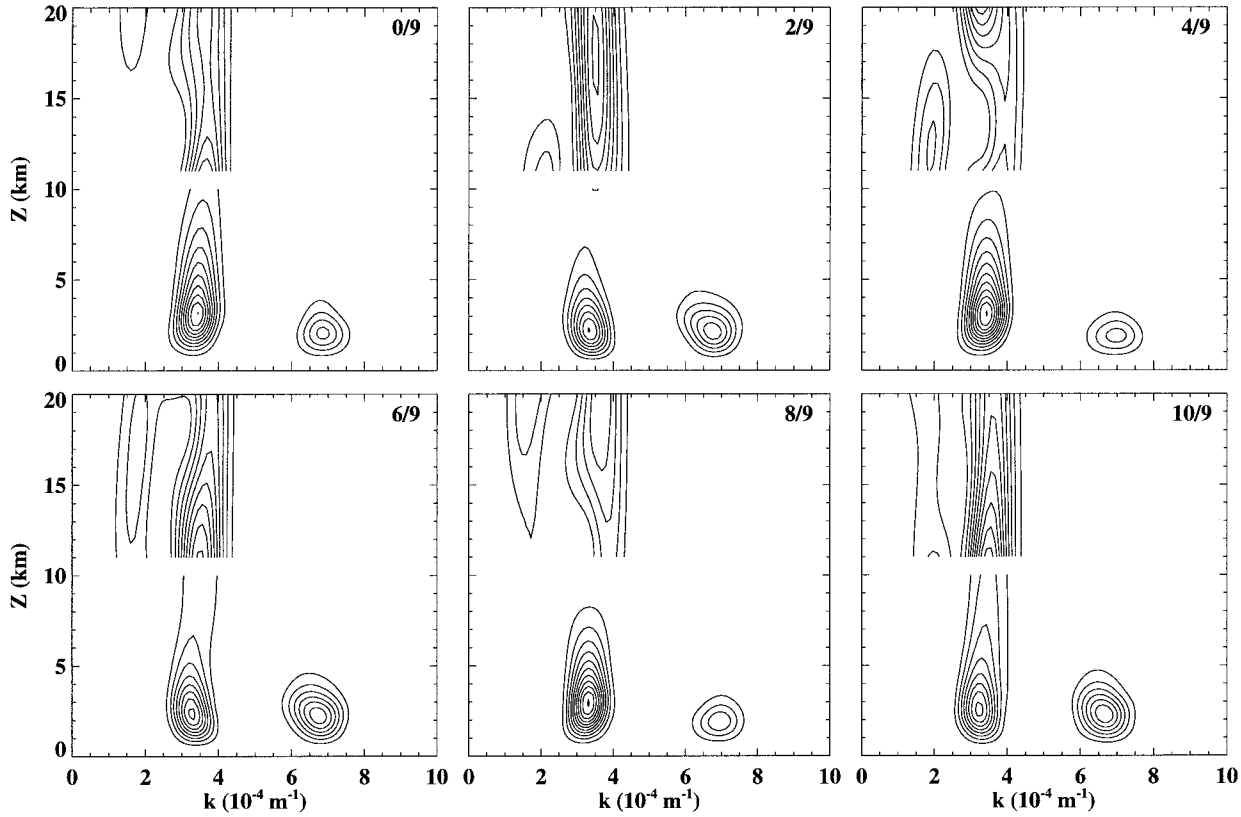

FIG. 5. Spectral power density as a function of horizontal wavenumber and height plotted every 1200 s between $t = 35\,400$ and 41 400 s. The contour interval below $z = 10$ km is 5 m^3 s^{-2}, and the contour interval above $z = 11$ km is 1 m^3 s^{-2}. The individual panels have been labeled by the fraction of one nonstationary wave period that has occurred since $t = 35\,400$ s. The time interval between each panel is approximately 2/9 of the period of the nonstationary waves.

power plotted as a function of horizontal wavenumber and vertical elevation are shown for six different times in Fig. 5. In order to better capture the weaker disturbance aloft, different contour intervals are used in the regions $0 \leq z \leq 10$ km and 11 km $\leq z \leq 20$ km. The time interval between each panel shown in Fig. 5 is 1200 s or approximately $\frac{2}{9}$ of a nonstationary wave period.

Three modes are prominent in Fig. 5. The vertically trapped mode with an average horizontal wavenumber of approximately 6.7×10^{-4} m^{-1} is the finite-amplitude manifestation of the stationary trapped wave predicted by linear theory (which in the linear Boussinesq limit would have a horizontal wavenumber of 6.75×10^{-4} m^{-1}). The upper-level mode with an average horizontal wavenumber of approximately 3.6×10^{-4} m^{-1} is the vertically propagating wave with the downstream phase speed evident in Fig. 4a. The vertically trapped mode with an average horizontal wavenumber of approximately 3.2×10^{-4} m^{-1} is primarily associated with the trapped wave that has the upstream phase speed evident in Fig. 4c. The horizontal wavenumber of the nonstationary trapped mode obtained from this spectral analysis appears to be shifted to a slightly higher wavenumber than that obtained from the analysis of Fig. 4 because the total spectral power in this portion of the k–z plane is also influenced by the higher wavenumber vertically propagating wave.

The structure of the vertically propagating wave becomes favorable for interaction with the trapped waves twice during each period of the nonstationary waves. Optimal phasing would occur when the vertical structures of all three modes are proportional to sin(mz) in the lower layer. One quarter-wave period after this optimal phasing, the vertically propagating wave would have a vertical structure proportional to cos(mz) in the lower layer, and the potential for interaction with the other modes would be minimal. As shown in Fig. 5, the spectral power in each of the three modes oscillates with twice the frequency of the nonstationary modes, suggesting that the strength of the nonlinear interaction is indeed modulated by changes in the phase of the vertically propagating wave.

At the start of one wave period (Fig. 5, panel 0/9), the power in the stationary trapped wave is near its minimum as energy appears to have been removed by interactions with the two other modes. A pulse of energy is just beginning to be carried into the upper layer by the vertically propagating wave. Approximately one quarter-wave period later (panel 2/9), there is much less

overlap of the spectral energy in the two nonstationary modes as a pulse representing the packet of higher-amplitude vertically propagating waves is now centered near a height of 18 km. Meanwhile, the spectral energy in the stationary trapped mode has increased. By the time shown in panel 4/9, wave–wave interactions appear to have once again depleted the energy in the stationary trapped mode, while amplifying the nonstationary trapped mode and initiating another pulse of energy in the vertically propagating mode. Meanwhile, the previous pulse of energy in the vertically propagating wave has continued to propagate upward, passed the 20-km level. This cycle continues as shown by the remaining panels in Fig. 5.

Although the cycle that transfers energy between the stationary and nonstationary modes clearly has two maxima every wave period, the odd and even phases of this cycle exhibit minor differences. Note, for example, that panel 0/9 more closely resembles 8/9 and 10/9 than panel 4/9. (Unfortunately, the times 4.5/9 and 9/9 are not available in the archived data.) This difference between the odd and even cycles in the energy transfer between the three modes may be related to the behavior of a fourth weaker mode with a horizontal wavenumber of approximately 2×10^{-4} m^{-1} that is visible in the upper layer. This mode appears to periodically transfer energy upward at a frequency similar to that of the dominant nonstationary modes. The spectral power in this fourth mode appears to be primarily associated with the vertically propagating waves forced directly by the mountain, as evidenced by the fact that the amplitude of this mode increases relative to the other modes when the horizontal domain over which the spectral analysis is performed is extended upstream to include the mountain. Since trajectories determined by the group velocity vectors for the vertically propagating waves originating at the mountain pass well above the region of lee-wave breakdown, these waves do not appear to play a major role in the generation of the nonstationary lee waves.

b. Sensitivities to changes in the nonstationary modes

Significant variations in the lee-wave structure appear to develop in the 385-m mountain simulation as a result of nonlinear interactions involving a stationary trapped wave of wavenumber k_s and two nonstationary waves with wavenumbers that are in close proximity to $k_s/2$. In this section, the role played by these nonstationary waves was further investigated by conducting a series of additional simulations in which the reference state is modified so that all waves with wavenumbers near $k_s/2$ are either trapped or vertically propagating. These modifications are made in such a manner that all the resulting atmospheric profiles support a linear stationary trapped wave with the same horizontal wavenumber as that in the REF case ($k_s = 6.75 \times 10^{-4}$ m^{-1}). The changes in the atmospheric profile were accomplished by either varying the jump in the Scorer parameter across the layer interface while keeping the depth of the lower layer constant or by changing the depth of the lower layer while keeping the jump in the Scorer parameter constant. Although the horizontal wavenumber of the linear stationary trapped wave is identical in all of the cases, other characteristics, such as the amplitude of the stationary trapped wave or its vertical structure, may differ from case to case [see Eq. (12) in Corby and Wallington (1956)]. Since the time dependence under investigation is a function of wave amplitude, the mountain height was normalized so that the amplitude of the linear stationary trapped wave in each case would be identical to the amplitude predicted by linear theory for flow over a mountain 385 m high in the REF case. The characteristics of each profile considered in this study are given in Table 2. In each case, the wind speed is 10 m s^{-1}, so the changes in l_l, l_u, and d are produced only by changes in the static stability profile.

TABLE 2. Characteristics of the two-layer profiles used in the numerical simulations. The amplitude factor is the ratio W_{REF}/W_i, where W_i is the maximum vertical velocity of the linear resonant waves generated by the basic-state flow i = *REF*, *IJ*, *DJT*, *DJU*, and *SJ* over a l-m-high mountain.

Profile	l_l^2 (m^{-2})	l_u^2 (m^{-2})	H (m)	k_{min}	Amplitude factor
REF	1.015×10^{-6}	1×10^{-7}	3000	1.7×10^{-4}	1
IJ	$1.04l \times 10^{-6}$	1.12×10^{-9}	3000	1.7×10^{-5}	0.935
DJT	1×10^{-6}	1.5×10^{-7}	3000	2.2×10^{-4}	1.04
DJU	9.4×10^{-7}	3×10^{-7}	3000	3.6×10^{-4}	1.27
SJ	1.15×10^{-6}	3×10^{-7}	2430	3.9×10^{-4}	0.94

First consider the increased jump case (IJ in Table 2), in which the Brunt–Väisällä frequency is increased slightly in the lower layer and reduced to 0.000355 s^{-1} in the upper layer. Under such circumstances, no gravity waves with horizontal wavenumbers near $k_s/2$ can propagate vertically in the upper layer, and, as shown by the x–z cross section of the vertical velocity field in Fig. 6a, no vertically propagating waves appear in the upper layer of the IJ simulation. Spatial variability similar to that shown for the REF case in Fig. 1b is, nevertheless, evident in the lee-wave train. The temporal variations in the IJ lee waves, which are shown by the x–t plot of the vertical velocity in Fig. 7a, are also similar to those shown for the REF case in Fig. 3b. One minor difference between Figs. 7a and 3b involves the leading edge of the region of lee-wave variability. In the IJ case, this leading edge appears to propagate downstream at an almost constant speed, whereas the leading edge of this region is less well defined in the REF case. In addition, the waves at the downstream edge are much weaker in the REF simulation, suggesting that energy lost through vertical transport has limited the overall width of the region of significant lee-wave variability. In contrast, the region of lee-wave variability may propagate downstream indefinitely when all of the energy in the inter-

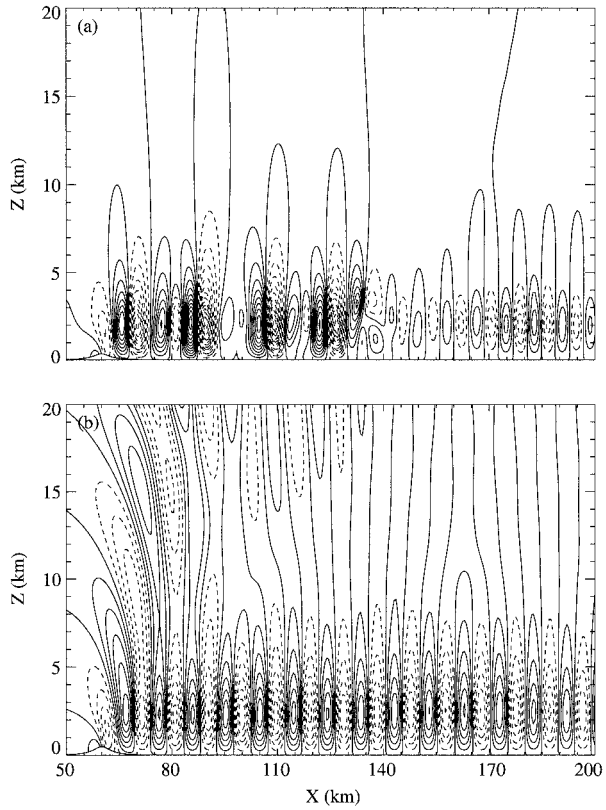

FIG. 6. Contour plots of the vertical velocity fields in the *x*–*z* plane at $t = 7$ h for the (a) IJ and (b) DJU profiles and a mountain height equivalent to 385 m. Contour interval is 0.5 m s^{-1}.

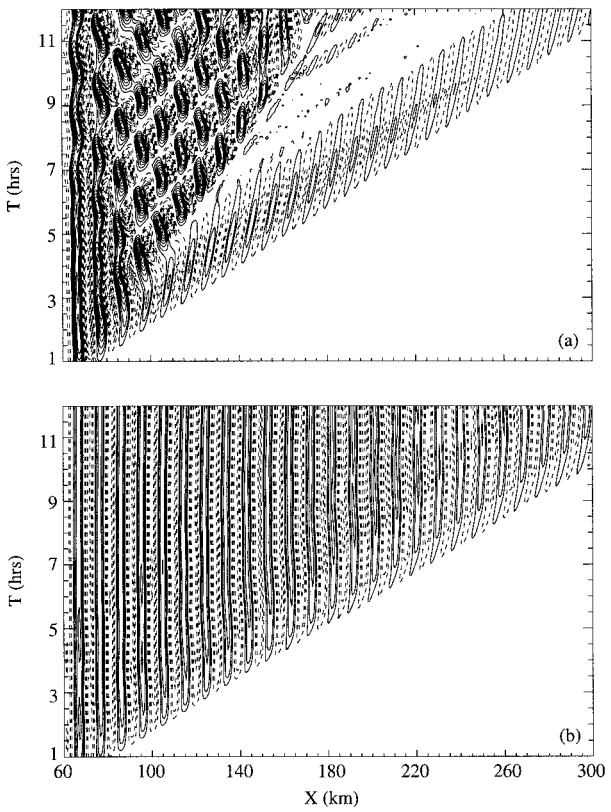

FIG. 7. Contour plots of the vertical velocity fields in the *x*–*t* plane at $z = 2$ km for the (a) IJ and (b) DJ profiles and a mountain height equivalent to 385 m. Contour interval is 0.7 m s^{-1}. The zero contour has been omitted for clarity.

acting waves is confined to modes that are vertically trapped.

The role played by the vertically propagating wave in the triad interaction in the REF case appears to be played by a second higher-order trapped mode in the IJ case. The phase speeds for the two lowest-order linear trapped modes supported by the IJ and REF cases are plotted as a function of horizontal wavenumber in Figs. 8a and 8b. The left edge of each curve terminates at the smallest wavenumber for which the corresponding profile supports a nonstationary trapped wave. Only one trapped mode can exist with a horizontal wavenumber near $k_s/2$ in the REF case, whereas two such modes can exist in the IJ case.

The horizontal wavenumber and frequency of the upstream propagating mode, determined from Fig. 7a, are approximately 3.6×10^{-4} m^{-1} and -0.0011 s^{-1}, respectively. The higher-order downstream propagating mode is hard to discern in the vertical velocity field shown in Fig. 7a, but it is evident in the *x*–*t* plot of the horizontal velocity perturbations shown in Fig. 9. The horizontal wavenumber and frequency of this mode, determined from Fig. 9, are approximately 3.2×10^{-4} m^{-1} and 0.0011 s^{-1}, respectively. The triad resonance criteria for the three trapped modes in the IJ case are approximately satisfied as follows:

horizontal wavenumber (in 10^{-4} m^{-1})

$$3.6 + 3.2 \approx 6.7,$$

frequency (in 10^{-3} s^{-1})

$$-1.1 + 1.1 = 0,$$

vertical wavenumber (in 10^{-4} m^{-1})

$$-6.9 + 14.4 \approx 7.7.$$

As before, the vertical wavenumbers have been computed from the horizontal wavenumbers and the frequencies using the linear Boussinesq dispersion relation. The signs of the vertical wavenumbers for these trapped waves are arbitrary and have been chosen to give approximate satisfaction of the resonant criteria. The criteria are once again satisfied to within $\pm 3\%$ of the largest term in each summation.

Now consider the case DJU in which the jump in the Scorer parameter across the layer interface is decreased sufficiently to untrap the mode with an upstream phase speed in the preceding simulations. Those horizontal wavenumbers for which nonstationary trapped waves can exist in the DJU case are plotted in Fig. 8c; note that all waves with horizontal wavenumbers less than 3.6×10^{-4} m^{-1} are vertically propagating. Elimination

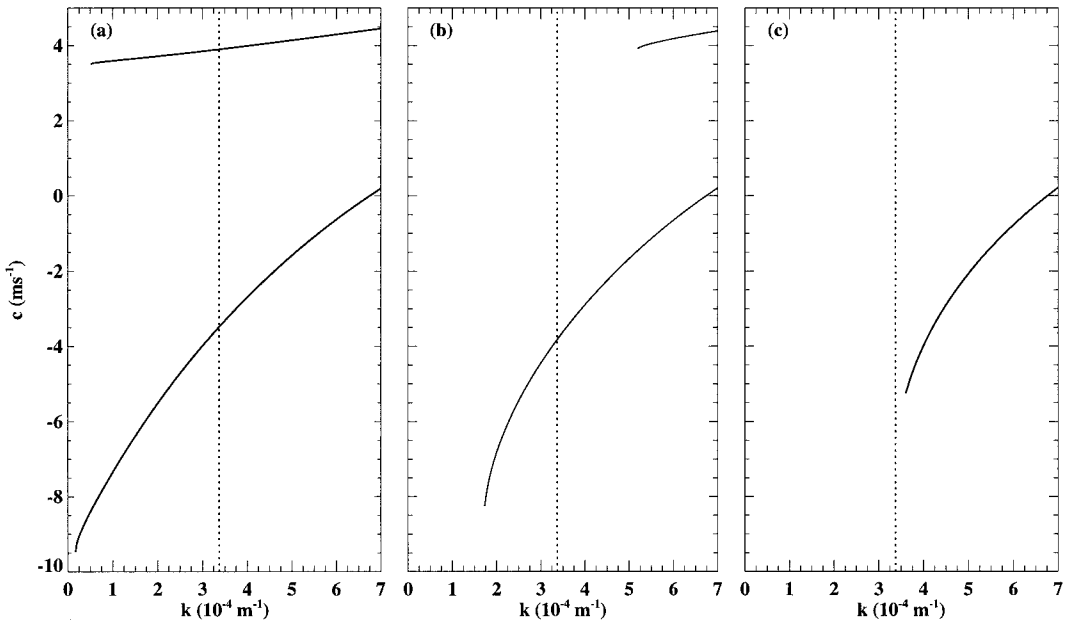

FIG. 8. The dispersion relation for the longest linear nonstationary trapped waves supported by the (a) IJ, (b) REF, and (c) DJU profiles. The dotted vertical line appears at $k = k_s/2$.

of the nonstationary trapped mode has drastically reduced the degree of spatial and temporal variability in the lee-wave train. As indicated in Fig. 6b, there is only a minor variation in the wave amplitude between adjacent troughs and crests, and, as shown in Fig. 7b, the temporal variations in the lee-wave train essentially disappear after the passage of the initial transients.

The other two cases indicated in Table 2 were also simulated. The case SJ, which does not support trapped waves with horizontal wavenumbers smaller than 3.9×10^{-4} m^{-1}, behaved similarly to case DJU. The lee-wave train (not shown) was essentially steady and almost perfectly regular. The case DJT, on the other hand, supports trapped waves with wavenumbers as small as 2.2×10^{-4} m^{-1}. Nonstationary perturbations developed in this case (not shown) that were similar to, but weaker than, those in the REF case. Based on the results obtained for these five cases, the most important atmospheric parameter governing lee-wave nonstationarity appears to be the ratio of the wavenumber of the stationary trapped wave to the cutoff wavenumber for which the profile will support a nonstationary trapped wave, k_{min}/k_s. When k_{min}/k_s is less than approximately one-half, nonstationary perturbations developed on the lee-wave train, and the degree of nonstationarity increased as k_{min}/k_s decreased. Conversely, when k_{min}/k_s exceeded one-half, the lee waves remained essentially stationary. It is not entirely clear why the interaction requires a trapped mode with a wavenumber near $k_s/2$ rather than a higher wavenumber, such as $2k_s/3$, since a vertically propagating wave can always be found whose frequency and horizontal wavenumber will satisfy the interaction criteria for the stationary trapped wave and an arbitrarily chosen trapped wave whose horizontal wavenumber is less than k_s. It may be that, whenever the horizontal wavenumbers of the nonstationary modes deviate significantly from $k_s/2$, the vertical wavenumbers become too incompatible to resonantly couple, but this hypothesis is not clearly supported by linear theory.

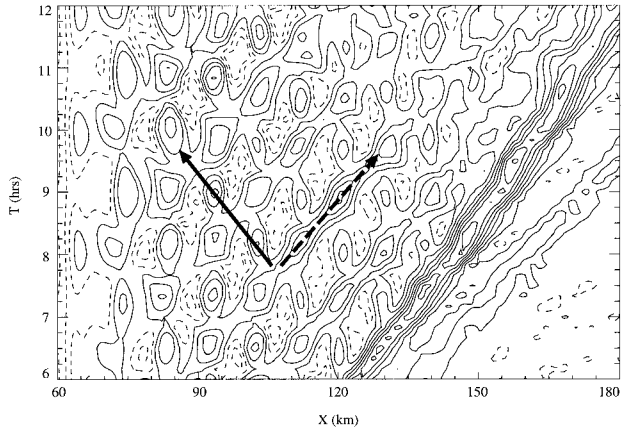

FIG. 9. As in Fig. 7a except contoured field is the negative of the perturbation horizontal velocity and the contour interval is 1 m s^{-1}. The solid and dashed arrows indicate phase speeds of -3 and 3.4 m s^{-1}, respectively.

In addition to its dependence on atmospheric structure, the degree of lee-wave nonstationarity is also a sensitive function of the strength of the topographic forcing in those cases where $k_{min}/k_s < 1/2$. Increasing the mountain height beyond that used in the preceding cases (or optimizing the mountain half-width to increase the forcing of the stationary trapped lee wave) leads to

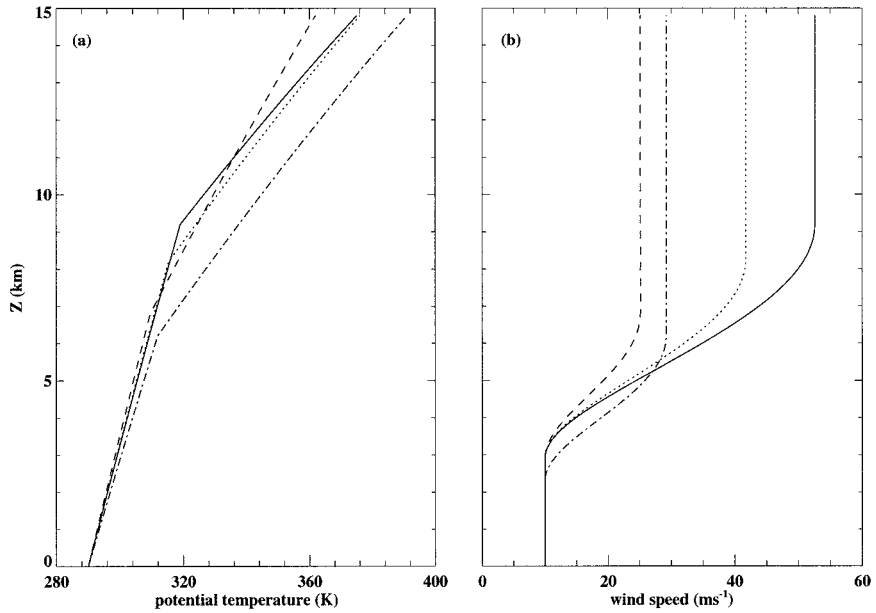

FIG. 10. Vertical profiles of (a) potential temperature and (b) wind speed for REFS (solid), DJTS (dotted), DJUS (dashed), and SJS (dot-dashed).

a more rapid breakdown of the stationary trapped wave and a more chaotic scattering of the spectral power over a wider range of horizontal wavenumbers. There was, however, no tendency for an increase in the height of the topography to produce nonsteady waves in those cases where $k_{\min}/k_s > 1/2$, unless the forcing became strong enough to generate wave breaking.

c. The effects of wind shear

For nonconstant wind speeds, the Scorer parameter for a compressible fluid can be well approximated as

$$l^2 = \frac{N^2}{\overline{u}^2} - 2\Gamma\frac{\overline{u}_z}{\overline{u}} - \frac{\overline{u}_{zz}}{\overline{u}}, \tag{4}$$

where

$$\Gamma = -\frac{d\ \ln\overline{\theta}}{dz} - \frac{1}{2}\frac{d\ \ln\overline{\rho}}{dz}$$

(Nance 1997). The sharp decrease in the Scorer parameter at the layer interface of Scorer's two-layer model can, therefore, be produced by a sharp increase in the curvature of the wind speed profile without any concomitant change in static stability. The vertical-velocity field associated with linear, steady-state, trapped lee waves is invariant to changes in the background flow that do not affect the Scorer parameter profile or the surface wind speed (Scorer 1949; Corby and Wallington 1956). Hence, the role of wind shear in finite-amplitude trapped lee-wave variability can be investigated by comparing pairs of numerical simulations with identical Scorer parameter configurations but different vertical profiles of wind speed and static stability. This study looked at four pairs that satisfy this criteria. The first member of each pair is one of the constant-wind-speed, two-layer static stability profiles listed in Table 2 (REF, DJT, DJU, and SJ). The second member of each pair has the same low-level static stability and surface wind speed, but, instead of a change in static stability at the interface between the two layers, the change in the Scorer parameter is produced entirely by changes in the wind speed. In addition, wind shear is eliminated near the upper boundary by setting $\overline{u}_z$ and $\overline{u}_{zz}$ to zero above the turning point in the wind profile (where $\overline{u}_z = 0$), while maintaining a constant Scorer parameter in the upper portion of the upper layer by changing the static stability to compensate for the elimination of wind shear. Eliminating wind shear near the upper boundary avoided the introduction of critical layers and numerical inaccuracies associated with the upper boundary condition. The potential temperature and wind speed profiles for the second member of each pair are shown in Fig. 10. The profiles with vertical wind shear will be referred to as REFS, DJTS, DJUS, and SJS.

Finite-amplitude trapped lee-wave simulations were computed for each wind shear profile using a mountain height scaled to produce the same linear response that would be obtained using the REF basic state and a mountain height of 385 m. The REFS and DJTS basic states generated nonstationary trapped lee-wave patterns with characteristics resembling those of their unsheared counterparts except that the nonstationary perturbations (both trapped and vertically propagating) are stronger in the sheared environment simulations. As an example, a comparison of the low-level wave patterns generated by the REF and REFS basic states between 1 and 6 h

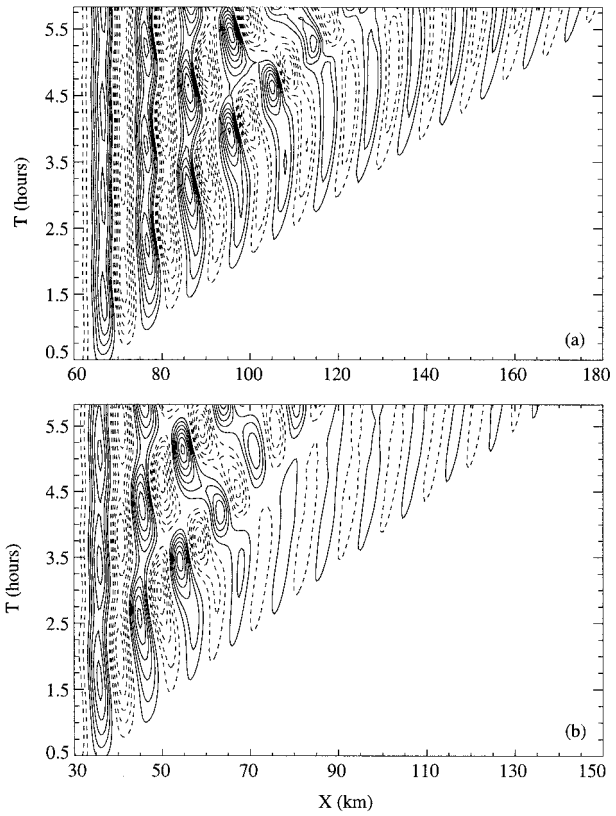

FIG. 11. Contour plots of the vertical velocity fields in the x–t plane at $z = 2$ km for (a) REF and (b) REFS profiles and a mountain height equivalent to 385 m. Contour interval is 0.7 m s^{-1}.

is shown in Fig. 11. In contrast, the basic states DJUS and SJS generated trapped lee waves that remained almost stationary throughout the simulation (not shown). At least in these experiments, wind shear increased any tendency toward nonstationarity that existed in the simulations conducted in the corresponding unsheared environment (profiles REF and DJT), but it did not generate nonstationarity in situations where the waves in the unsheared environment were steady (profiles DJ and SJ).

4. Observed atmospheric profiles

Many lee-wave observations are gathered in a manner that makes it difficult to determine the extent to which the waves are nonstationary. For instance, some observational studies use data collected at a single time, such as a solitary satellite image of lee-wave clouds, while other studies use data collected over time periods on the order of 1–4 h by instruments, such as radar-tracked superpressure balloons, radiosondes, or instrumented aircraft, traveling through the wave pattern. Data collected by a single instrument traveling through a train of nonstationary waves contain signals arising from the wave train's temporal and spatial structures, but the signal arising from the temporal structure may be impossible to separate from that arising from the spatial structure. In this section, we consider two cases in which the observed waves exhibited what appears to be a mixture of temporal and spatial variability. Our goal is to demonstrate that actual atmospheric soundings are capable of generating nonstationary lee-wave trains through nonlinear wave dynamics. Rather than conducting detailed case studies using a close approximation to the actual topographic profile, we utilize idealized topographic profiles whose maximum height is less than or equal to the height of the actual topography.

a. Reynolds et al. (1968)

On 6 May 1965, radar-tracked superpressure balloons recorded a well-defined wave system with variable wavelength and amplitude over, and in the lee of, the San Andres Mountains of southern New Mexico at a mean altitude of approximately 3.5 km. The trough to trough wavelengths of the three waves observed downstream of the topography were 9.8, 9.4, and 11.3 km, respectively (Reynolds et al. 1968, Fig. 1). This type of wavelength variation between adjacent waves together with the observed amplitude variations resembles the wavelength and amplitude variations in the nonstationary lee-wave patterns generated by nonlinear effects in the preceding two-layer flows. The superpressure balloon took approximately 50 min to traverse the three waves downstream of the mountain, so the lee-wave pattern documented by the superpressure balloon measurements is likely to reflect a combination of spatial and temporal variability.

The basic-state environment in the numerical simulation for this case was specified using data collected by a rawinsonde released 12.8 km south of the balloon track. Since solar insolation probably eliminated the shallow nocturnal inversion in this sounding by the time the waves were observed, this inversion was removed by extending the lapse rate above the inversion layer down to the surface. The wind speed, potential temperature, and Scorer parameter profiles of this background flow are shown in Fig. 12. The Scorer parameter profile is a maximum in the stable layer around a height of 2 km and then drops to almost zero between 4.5 and 7.5 km. The larger Scorer parameter values above 8 km allow the low-wavenumber trapped modes to leak energy into the stratosphere.

As indicated in Fig. 13, a numerical simulation using this steady background flow generated a clearly nonstationary lee-wave train downstream of a Witch of Agnesi mountain 800 m high.[1] The trough to trough wavelengths in this nonstationary lee-wave pattern vary from 9 to 12 km, which agrees with the variability in the lee-wave pattern documented by the superpressure balloons.

[1] The maximum height of the actual topography was 1200 m.

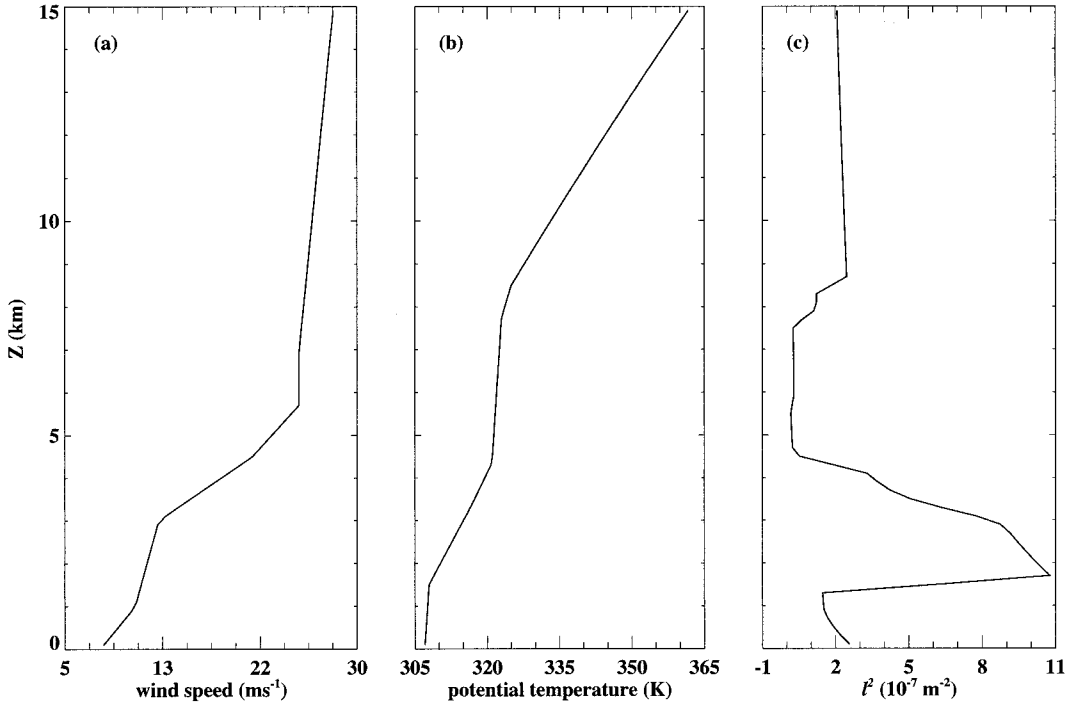

FIG. 12. The (a) horizontal wind speed, (b) potential temperature, and (c) Scorer parameter profiles of the basic state based on the background conditions from Reynolds et al. (1968).

The details of the observed and simulated waves do, however, differ in two respects. First, the lee-wave wavelength begins to vary immediately downstream of the mountain in the observations, whereas the region of pronounced variability in the numerical simulation appears farther downstream. Second, a wave appears upstream of the main topographic crest in the observations but is absent in the simulations. Some of the differences between the observations and the simulations are due to the simplified topography used in the numerical simulations, which does not account for the complexity of the San Andres Mountains and the smaller ridges upstream of the main mountain crest. Due to the spotty coverage of the superpressure balloon observations and

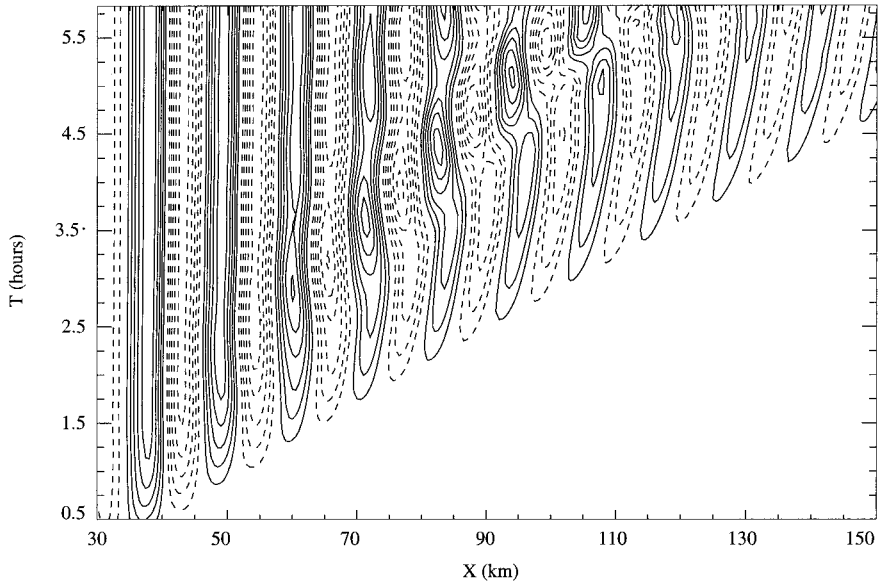

FIG. 13. Contour plot of the vertical velocity field in the x–t plane at $z = 3$ km for the profile from Reynolds et al. (1968) and a mountain height of 800 m. Contour interval is 1.2 m s^{-1}.

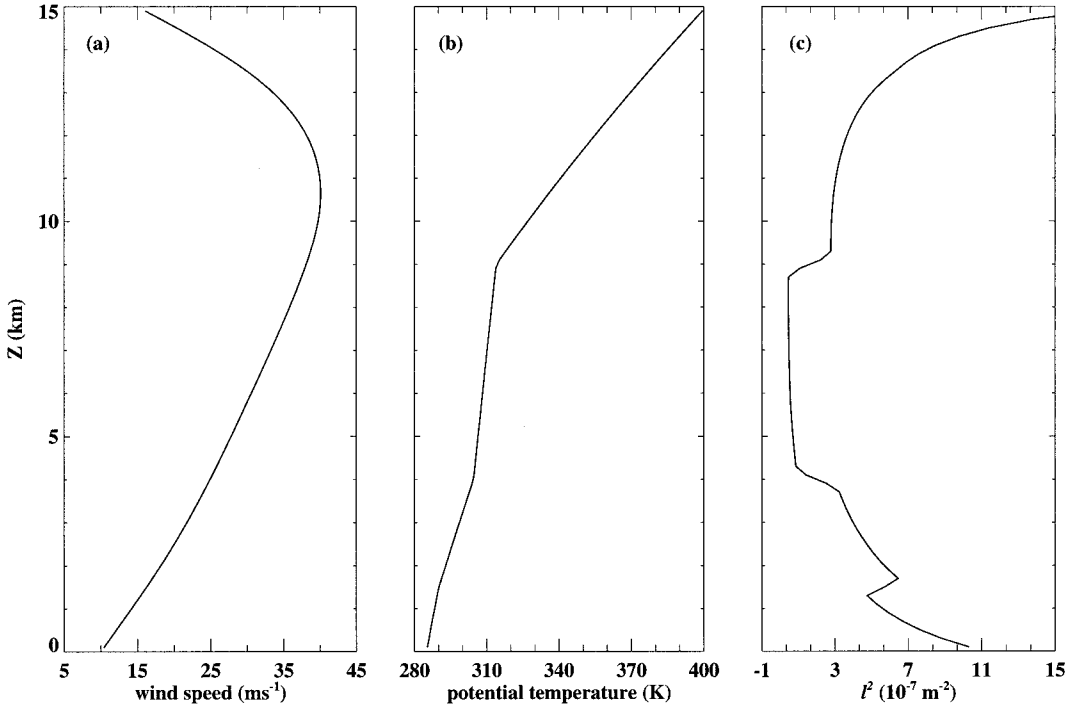

FIG. 14. The (a) horizontal wind speed, (b) potential temperature, and (c) Scorer parameter profiles of the basic state used to simulate the large-scale features of the background conditions associated with the lee-wave event documented by Shutts and Broad (1993).

the lack of data on the upstream topographic effects, a more detailed comparison between the numerical simulation and the observations is not possible. Nevertheless, this simulation demonstrates that a steady background flow with the vertical structure documented by Reynolds et al. (1968) will support the growth of nonstationary perturbations on finite-amplitude trapped mountain lee waves.

b. Shutts and Broad (1993)

On 26 November 1991 a satellite photograph revealed cloud bands formed by lee waves with variable spacing over the Lake District in northern England. Shutts and Broad (1993) determined the detailed structure of these waves using five radiosondes with different ascent rates released in rapid succession and an aircraft flying tracks approximately 160 km long at four different altitudes. Vertical coherence in the vertical velocity, a signature of trapped waves, was readily detectable on the lowest two flight tracks, except in a region 70–100 km downstream. Crests and troughs in the vertical velocity signature were displaced by as much as 5 km in this region. The aircraft traversed each 160-km track in approximately 30 min, starting at the lowest level and retracing the path in the opposite direction at each successive level. This flight pattern created a lag time of approximately 30 min between the observations recorded on the lowest two aircraft flight tracks in the region that lacked vertical coherence, so the breakdown in the coherence of the vertical velocity in this region may be related to wave transience. A composite of the radiosonde ascents and the aircraft measurements produced a lee-wave pattern with a dominant horizontal wavelength of approximately 20 km and an amplitude maximum at about 3 km with vertical velocities up to 3.5 m s^{-1}. The phase lines were tilted upstream with height above 5 km, suggesting energy leakage to the stratosphere.

The wind speed, potential temperature, and Scorer parameter profiles of the basic state used in the numerical simulation for this event are shown in Fig. 14. The large-scale features of the observed wind speed profile were extracted by fitting a cubic spline to the data. The lowest Scorer parameter values in the background flow were located in an intermediate layer between 4 and 9 km, while the largest values were located at upper levels. As indicated in Fig. 15, a numerical simulation using this steady background flow generated a vigorous nonstationary lee-wave train downstream of a Witch of Agnesi mountain 600 m high.[2] This nonstationarity gradually increases with distance downstream of the mountain until it becomes significant around 100 km (70 km downstream of the mountain peak). The

[2] The actual topography has a maximum height of almost 900 m.

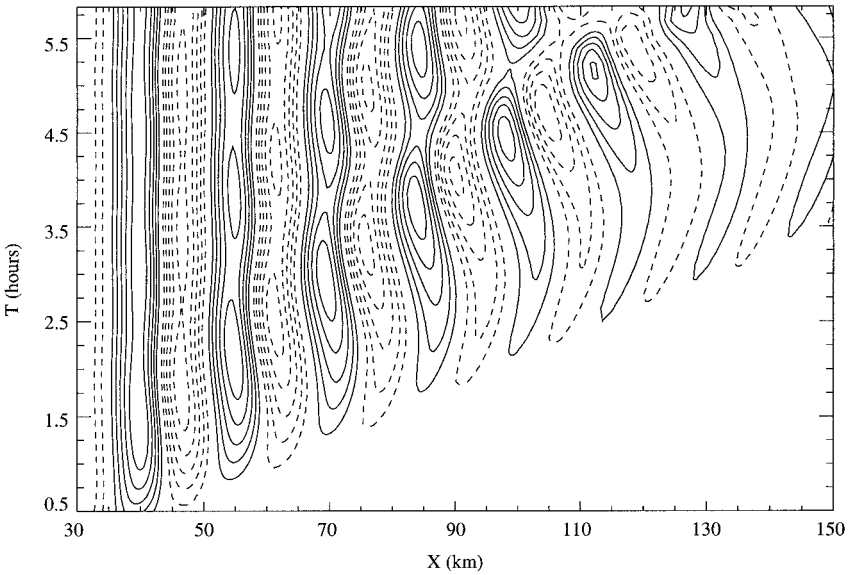

FIG. 15. Contour plot of the vertical velocity field in the x–t plane at $z = 3.8$ km for the profile from Shutts and Broad (1993) and a mountain height of 600 m. The contour interval is 1.0 m s^{-1}.

nonstationarity between 100 and 130 km can account for the displacement of a crest or trough in the lee-wave pattern on the order of 4 km over a 30-min time period. The flight pattern for the two lowest levels was such that observations immediately in the lee of the mountain were separated by almost an hour, whereas the observations in the region 160 km downstream of the mountain were separated by minutes. The relative stationarity of the first few waves immediately downstream of the mountain in the numerical simulation could account for the vertical coherence in the observations between 0 and 70 km. Due to the time lag, the nonstationary response in the numerical simulation could account for the degradation of vertical coherence in the observations between 70 and 100 km. Finally, the small time lag near the downstream boundary of the flight track could account for the vertical coherence in the observations between 100 and 160 km. The characteristics of the observed vertical velocity field are, therefore, roughly consistent with the nonstationary behavior in the numerical simulation. In any case, this simulation demonstrates that a steady background flow with the large-scale vertical structure documented by Shutts and Broad (1993) is capable of generating nonstationary trapped mountain lee waves.

5. Wind profiler observations

In contrast to superpressure balloon and instrumented aircraft observations, wind-profiler-observed vertical motions provide an unambiguous description of the temporal fluctuations in wave-induced vertical motions above a single point. Recent observational studies have found that wind-profiler-observed vertical motions related to nonstationary lee-wave events can exhibit temporal oscillations with periods ranging from slightly less than 1 h to almost 4 h (Ralph et al. 1992; Bougeault et al. 1993). Figure 13 in Bougeault et al. (1993) shows an example of such wind-profiler-observed vertical motions (alternatively, see Fig. 10 in ND97). The vertical motions in this particular time series oscillate with a period of roughly 2 h, and the temporal variations between 0500 and 0630 UTC appear to contain a secondary oscillation with a period of approximately 30 min. Although it is difficult to quantitatively compare numerical simulations and observations above a fixed point, it is possible to qualitatively compare the characteristics of wind-profiler-observed vertical motions and the evolving vertical velocity fields in numerical simulations. Using time series of vertical velocity profiles from idealized time-dependent flow simulations, ND97 showed that a very rapidly varying mean flow can generate temporal oscillations in wave-induced vertical velocities above a single point that roughly agree with wind profiler observations. Details of the observed response, such as the short period secondary oscillation in the vertical velocity were not, however, generated by variations in the mean flow.

Wind profilers sampling the trapped waves at $x = 61$ km and $x = 63$ km (31 km and 33 km downstream of the mountain ridge) in a numerical simulation for a steady background flow defined by the DJT profile and a mountain 600 m high would have recorded the vertical velocities shown in Fig. 16. The vertical velocities at $x = 61$ km change sign with time, whereas the vertical velocities at $x = 63$ km remain negative after the arrival of the stationary trapped wave ($t > 3$ h). This dependence on the location of the wind profiler is due to the

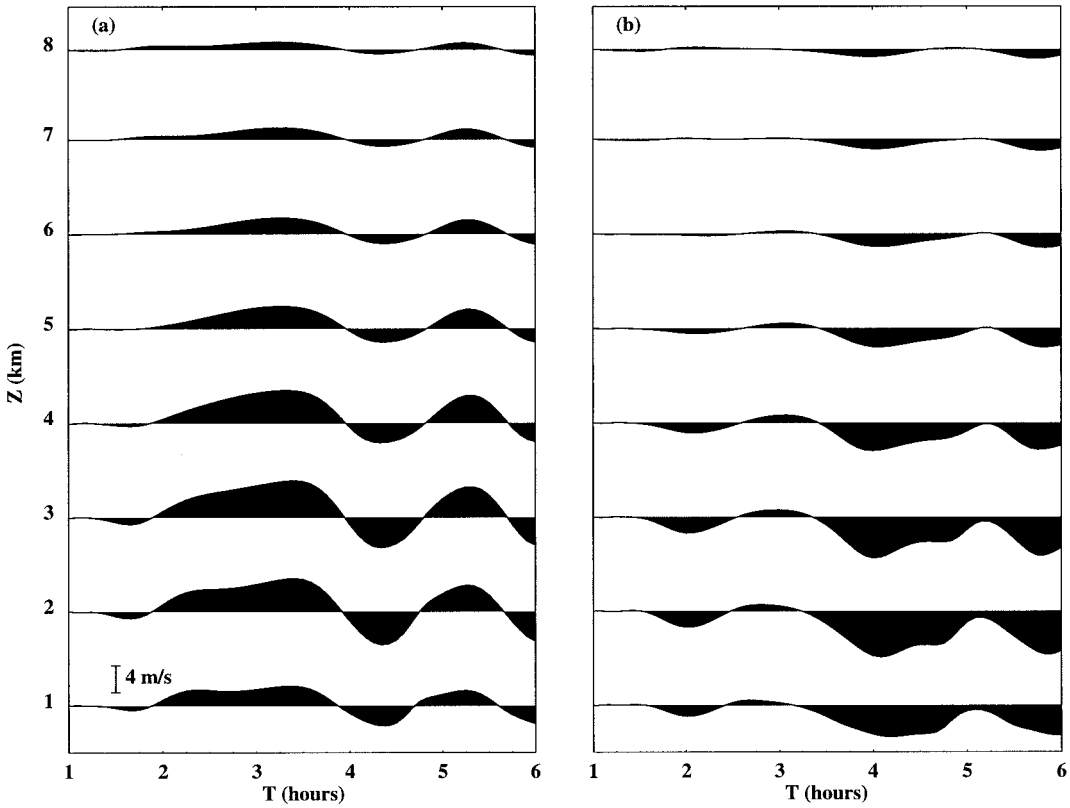

FIG. 16. Time series of the vertical velocity above a site located (a) 31 km ($x = 61$ km) and (b) 33 km ($x = 63$ km) downstream of the mountain peak at eight different elevations for the mountain wave simulation with a mountain height of 600 m and the DJT profile.

fact that $x = 61$ km roughly corresponds to a node in the stationary component of the wave pattern, whereas $x = 63$ km roughly corresponds to a trough in the stationary component. The temporal variations in both of these time series are dominated by oscillations with a period of roughly 2 h, but between 4 and 5 h the vertical velocities at $x = 63$ km also contain a signature of an oscillation with a period of slightly less than 1 h. Note the similarity between this temporal behavior and that observed downstream of the Pyrenees Mountains on 15 October 1981 between 0500 and 0630 UTC (see Fig. 10 in ND97). This similarity suggests that nonlinear wave dynamics may have been responsible for the secondary oscillation in these lee-wave vertical velocities.

6. Conclusions

Linear theory predicts that trapped mountain lee waves generated by a steady background flow will become stationary after the decay of an initial transient. This result need not hold, however, at finite amplitude. As demonstrated in this study, finite-amplitude trapped lee waves may exhibit temporal variations in local wavelength and amplitude, even when the background flow is perfectly steady. These variations may appear as regular oscillations in which the crests and troughs of the trapped lee waves trace elliptical paths in the x–z plane. The oscillations of adjacent crests are 180 degrees out of phase, thereby producing a systematic variation in local wavelength and amplitude. The nonstationary perturbations become stronger and more irregular as the wave amplitude increases, and they may dominate the overall wave pattern at wave amplitudes significantly below the threshold required to produce wave breaking.

For moderate amplitudes, the development of nonstationary perturbations on the stationary trapped wave appears to involve an interaction between the stationary trapped wave and two longer-wavelength nonstationary waves. This pair of nonstationary waves can be composed of either two trapped waves or a trapped wave and a vertically propagating wave. A series of numerical simulations were conducted in which the wave propagation characteristics of the background flow were varied without changing the wavelength of the stationary trapped mode predicted by linear theory. The simulated finite-amplitude lee waves developed nonstationary perturbations in those cases where the background flow supported nonstationary trapped waves with horizontal wavelengths approximately twice that of the stationary trapped wave, whereas the simulated lee waves remained stationary in those cases where all waves with

horizontal wavelengths twice that of the stationary trapped wave propagated vertically.

Simulations were also conducted using sounding data collected in connection with two observed lee-wave events that showed some evidence of lee-wave variability. No attempt was made to simulate all the details of each observed event. The background flow for each numerical simulation was defined using a smooth fit to the observed temperature and wind speed sounding, and the topography was specified as an isolated Witch of Agnesi mountain. In both cases, the numerically simulated lee waves developed nonstationary perturbations similar to those that developed in the idealized two-layer flows. The variations in the lee waves increased with wave amplitude and became pronounced before the height of the Witch of Agnesi mountain equaled that of the actual topography. These simulations demonstrate that nonlinear wave dynamics provide a viable mechanism for generating nonsteady lee waves in real atmospheric situations without any concomitant variations in the background flow.

In Part I of this study, it was demonstrated that changes in the background flow can also produce irregular variations in lee-wave wavelength and amplitude if the group of waves generated after the change in the background flow overtake those generated prior to the change in the background flow. It appears, however, that in order to generate irregular variations in the wave train through this mechanism, the background flow must change on an unrealistically rapid timescale. Moreover, the change in the background flow must be somewhat special in that it must change the horizontal wavelength of the stationary trapped mode without significantly modifying the wave amplitude. As demonstrated in Part II of this study, irregular variations in lee-wave wavelength and amplitude can be generated solely by nonlinear wave dynamics without requiring a rapid change between two specially tuned basic states. The irregular variations in lee-wave wavelength and amplitude observed in real atmospheric flows may often be generated by nonlinear wave dynamics rather than by changes in the background flow.

Fine temporal resolution observations of vertical velocities above a single fixed point that are associated with trapped mountain lee waves have been obtained using VHF profilers. Occasionally these observations show a relatively complex series of fluctuations (Bougeault et al. 1993) that appear to be a superposition of waves with several different periods. This study showed that nonlinear wave dynamics can generate a wider range of nonstationary trapped modes than a simple change in the background flow. The presence of these additional modes can, in turn, produce fluctuations in the vertical velocity above a single fixed point that more closely match the relatively complex series of fluctuations occasionally found in wind-profiler-observed vertical velocities.

Acknowledgments. We would like to thank Dr. James Holton and Dr. Christopher Bretherton for their suggestions and comments throughout this project. This work was supported by the National Science Foundation Grants ATM-8813971, ATM-9218376, and ATM-9322480.

APPENDIX

Description of Power Spectrum Calculations

The horizontal wavenumber power spectra considered in this study were computed using the following procedure. Horizontal cross sections of the w field were taken at each model level in the region of interest. A Welch window, defined by

$$W_j = 1 - \left(\frac{j - \frac{1}{2}(n-1)}{\frac{1}{2}(n+1)} \right)^2 \quad \text{for } 1 \le j \le n, \tag{A1}$$

where n represents the number of data points in the cross section, was applied to the data, and the data array was padded with zeroes to obtain an array of 1024 elements. The application of the window function reduces the spread of the signal due to the finiteness of the record. Zero padding increases the resolution of the wavenumber bins in the discrete Fourier transform. A discrete Fourier transform was applied to these arrays and the power spectral density was computed at each level using the formulas

$$\text{psd}(0) = \frac{1}{W_s}[\hat{w}_r^2(0) + \hat{w}_i^2(0)]\frac{n}{n_t} \tag{A2}$$

and

$$\text{psd}(k) = \frac{2}{W_s}[\hat{w}_r^2(\text{k}) + \hat{w}_i^2(\text{k})]\frac{n}{n_t} \tag{A3}$$

for $2\pi/n\Delta x \le k \le \pi/\Delta x$. In the above, $\hat{w}_r$ and $\hat{w}_i$ represent the real and imaginary components of the amplitude of the kth component of the Fourier decomposition of w, respectively; n_t represents the number of points in the zero-padded array; and W_s is defined by

$$W_s = \sum_{j=1}^{n} W_j^2. \tag{A4}$$

This power spectral density is based on the sum-squared amplitude description of the total power (Jenkins and Watts 1968; Press et al. 1986).

REFERENCES

Bougeault, P., 1983: A nonreflective upper boundary condition for limited-height hydrostatic models. *Mon. Wea. Rev.*, **111,** 420–429.

——, A. Jansa, J. L. Attie, I. Beau, B. Benech, R. Beniot, P. Bessemoulin, J. L. Caccia, J. Campins, B. Carissimo, J. L. Cham-

peaux, M. Crochet, A. Druilhet, P. Durand, A. Elkhalfi, P. Flamant, A. Genoves, M. Georgelin, K. P. Hoinka, V. Klaus, E. Koffi, V. Kotroni, C. Mazaudier, J. Peon, M. Petitdidier, Y. Pointin, D. Puech, E. Richard, T. Satomura, J. Stein, and D. Tannhauser, 1993: The atmospheric momentum budget over a major mountain range: First results of the PYREX field program. *Ann. Geophys.,* **11,** 395–418.

Brown, P. R. A., 1983: Aircraft measurements of mountain waves and their associated momentum flux over the British Isles. *Quart. J. Roy. Meteor. Soc.,* **109,** 849–865.

Collis, R. T. H., F. G. Fernald, and J. E. Alder, 1968: Lidar observations of Sierra wave conditions. *J. Appl. Meteor.,* **7,** 227–233.

Colson, D., and C. V. Lindsay, 1959: Unusual wave cloud over Washington, D.C., November 30, 1959. *Mon. Wea. Rev.,* **87,** 451–452.

Corby, G. A., and C. E. Wallington, 1956: Airflow over the mountains: The lee wave amplitude. *Quart. J. Roy. Meteor. Soc.,* **82,** 266–274.

Durran, D. R., and J. B. Klemp, 1982: The effects of moisture on trapped mountain lee waves. *J. Atmos. Sci.,* **39,** 2490–2506.

——, and ——, 1983: A compressible model for the simulation of moist mountain waves. *Mon. Wea. Rev.,* **111,** 2341–2361.

Hasselmann, K., 1967: A criterion for nonlinear wave stability. *J. Fluid Mech.,* **30,** 737–739.

Jenkins, G. M., and D. G. Watts, 1968: *Spectral Analysis and Its Applications.* Holden Day, 525 pp.

Klemp, J. B., and D. R. Durran, 1983: An upper boundary condition permitting internal gravity wave radiation in numerical mesoscale models. *Mon. Wea. Rev.,* **111,** 430–444.

Lindsay, C. V., 1962: Mountain waves in the Appalachians. *Mon. Wea. Rev.,* **90,** 271–276.

Mitchell, R. M., R. P. Cechet, P. J. Turner, and C. C. Elsum, 1990: Observation and interpretation of wave clouds over Macquarie Island. *Quart. J. Roy. Meteor. Soc.,* **116,** 741–752.

Nance, L. B., 1997: On the inclusion of compressibility effects in the Scorer parameter. *J. Atmos. Sci.,* **54,** 362–367.

——, and D. R. Durran, 1997: A modeling study of nonstationary trapped mountain lee waves. Part I: Mean flow variability. *J. Atmos. Sci.,* **54,** 2275–2291.

Pandya, R. E., and D. R. Durran, 1996: The influence of convectively generated thermal forcing on the mesoscale circulation around squall lines. *J. Atmos. Sci.,* **53,** 2924–2951.

Press, W. H., B. P. Flannery, S. A. Teukolsky, and W. T. Vetterling, 1986: *Numerical Recipes: The Art of Scientific Computing.* Cambridge University Press, 818 pp.

Queney, P., G. Corby, N. Gerbier, H. Koschmieder, and J. Zierep, 1960: The airflow over mountains. World Meteorological Organization Tech. Note 34, 135 pp. [Available from WMO, Case Postale 2300, CH-1211 Geneva 2, Switzerland.]

Ralph, F. M., M. Crochet, and S. V. Venkateswaran, 1992: A study of mountain lee waves using clear-air radar. *Quart. J. Roy. Meteor. Soc.,* **118,** 597–627.

——, P. J. Neiman, T. L. Keller, D. Levinson, and L. Fedor, 1997: Observations, simulations, and analysis of nonstationary trapped lee waves. *J. Atmos. Sci.,* **54,** 1308–1333.

Reynolds, R. D., R. L. Lamberth, and M. G. Wurtele, 1968: Investigation of a complex mountain wave situation. *J. Appl. Meteor.,* **7,** 353–358.

Sarker, R. P., and R. V. Calheiros, 1974: Theoretical analysis of lee waves over the Andes as seen by satellite pictures. *Pure Appl. Geophys.,* **112,** 301–319.

Scorer, R., 1949: Theory of waves in the lee of mountains. *Quart. J. Roy. Meteor. Soc.,* **75,** 41–56.

Shutts, G. J., and A. Broad, 1993: A case study of lee waves over the Lake District in northern England. *Quart. J. Roy. Meteor. Soc.,* **119,** 377–408.

Smith, R. B., 1976: The generation of lee waves by the Blue Ridge. *J. Atmos. Sci.,* **33,** 507–519.

Starr, J. R., and K. A. Browning, 1972: Observations of lee waves by high-power radar. *Quart. J. Roy. Meteor. Soc.,* **98,** 73–85.

Wurtele, M. G., 1955: The transient development of a lee wave. *J. Mar. Res.,* **14,** 1–13.

——, R. D. Sharman, and T. L. Keller, 1987: Analysis and simulations of a troposphere-stratosphere gravity wave model. Part I. *J. Atmos. Sci.,* **44,** 3269–3281.